Nanoscale

ROYAL SOCIETY OF CHEMISTRY

PAPER

View Article Online
View Journal

Cite this: DOI: 10.1039/d2nr06632g

Reaction stoichiometry directs the architecture of trimetallic nanostructures produced *via* galvanic replacement†

Nabojit Kar, [a] Maximilian McCoy, [a] Xun Zhan, [a] Joshua Wolfe, [a] Zhiyu Wang [b] and Sara E. Skrabalak *[a]

Received 27th November 2022,
Accepted 9th January 2023

DOI: 10.1039/d2nr06632g

rsc.li/nanoscale

Galvanic replacement (GR) of monometallic nanoparticles (NPs) provides a versatile route to interesting bimetallic nanostructures, with examples such as nanoboxes, nanocages, nanoshells, nanorings, and heterodimers reported. The replacement of bimetallic templates by a more noble metal can generate trimetallic nanostructures with different architectures, where the specific structure has been shown to depend on the relative reduction potentials of the participating metals and lattice mismatch between the depositing and template metal phases. Now, the role of reaction stoichiometry is shown to direct the overall architecture of multimetallic nanostructures produced by GR with bimetallic templates. Specifically, the number of initial metal islands deposited on a NP template depends on the reaction stoichiometry. This outcome was established by studying the GR process between intermetallic PdCu (i-PdCu) NPs and either $AuCl_2^-$ (Au^{1+}) or $AuCl_4^-$ (Au^{3+}), producing i-PdCu–Au heterostructures. Significantly, multiple Au domains form in the case of GR with $AuCl_2^-$ while only single Au domains form in the case of $AuCl_4^-$. These different NP architectures and their connection to reaction stoichiometry are consistent with Stranski–Krastanov (SK) growth, providing general guidelines on how the conditions of GR processes can be used to achieve multimetallic nanostructures with different defined architectures.

Introduction

Nanoparticle (NP) heterostructures are an important class of nanomaterials, with applications in fuel-cell catalysis,[1,2] plasmonics,[3] solar cells,[4] electronics,[5,6] and even as theranostics.[7,8] NP heterostructures consist of two or more material domains joined together in a single NP, where electronic exchange between the materials is possible and the created interface can impart important functionality.[9] For instance, Zhu *et al.* synthesized bifunctional Fe_3O_4–AgI heterodimers, where the magnetic Fe_3O_4 domain enables magnetic resonance imaging while the AgI domain provides iodine-125 as a single photon emitting radionucleotide for photon emission computed tomography.[10] As a second example, Ding *et al.* synthesized Pt–CuS NP heterostructures with high activity and selectivity for catalyzing the methanol oxidation reaction.[11] The high catalytic activity was attributed to the strong electronic coupling between the two domains.

Many colloidal techniques, including seed-mediated growth,[12] ligand-mediated self-assembly,[13] and electrostatic assembly[14] can be used to create NP heterostructures. In seed-mediated growth, a new material domain can grow at a specific site of a pre-existing NP, whereas assembly approaches connect preformed NPs together.[15,16] The form of heterostructured NPs (*i.e.*, their architecture) can be influenced by different capping agents in addition to the barriers for interface formation and adatom diffusion.[12]

Despite such progress, independent control of the number of domains and interfaces within NP heterostructures remains challenging. This synthetic hurdle arises from the complexity of the reaction media.[17] Here, we exploit galvanic replacement (GR) to prepare compositionally complex metal NP heterostructures and test the hypothesis that the overall NP architecture depends on the reaction stoichiometry of the GR process. The GR process with NP templates is an exciting pathway to NP heterostructures given its predictable redox chemistry in which metal ions with higher reduction potentials (more noble) than those in the metal NP templates undergo reduction and replacement.[18] A classic example is the replacement of Ag nanocubes with Au, forming AuAg nanocages.[19]

---

[a] Department of Chemistry, Indiana University – Bloomington, 800 E. Kirkwood Ave., Bloomington, Indiana 47405, USA. E-mail: sskrabal@indiana.edu
[b] Materials Research Laboratory, University of Illinois at Urbana-Champaign, 104 S. Goodwin Ave., Urbana, Illinois 61801, USA

† Electronic supplementary information (ESI) available: Low magnification TEM images, elemental and phase characterizations, tomograms, summary tables. See DOI: **https://doi.org/10.1039/d2nr06632g**

Since this early demonstration, GR with various NP templates has been used to generate a variety of complex NPs such as alloy nanoshells (hollow structures),[20] nanocages (porous, hollow structures),[19] and even nanotadpoles,[21] dimers,[22] and trimetallic nanorods.[23] Factors that contribute to whether alloy NPs or NP heterostructures form through GR include the rate of adatom generation,[24] the barrier for adatom diffusion on the template NP,[25] and the barrier to interdiffusion.[18]

Recently, GR has been applied to less conventional NP templates. For example, Castilla-Amorós *et al.* synthesized copper–gallium (Cu–Ga) nanodimers by GR of liquid Ga templates (Ga^{3+}/Ga E_{red} = −0.53 V *vs.* SHE) with Cu (Cu^{2+}/Cu E_{red} = +0.34 V *vs.* SHE).[22] The formation of nanodimers instead of alloys was attributed to the migration of Ga atoms through the native gallium oxide shell, which separates the depositing Cu from Ga and hinders the alloying process. Likewise, our group studied GR between intermetallic PdCu (i-PdCu) NPs and either $AuCl_4^-$ or $PtCl_6^{2-}$, where these salts can oxidize both Pd and Cu in the template NPs based on their standard reduction potentials.[26] Notably, titrating with $AuCl_4^-$ produced Janus-style i-PdCu–Au heterodimers while core@shell i-PdCu@PtPd NPs were produced with $PtCl_6^{2-}$ as the titrant.[26] The rationale behind the different products was the much slower surface mobility of Pt adatoms compared to Au adatoms and highlights how different NP architectures are possible with GR.

In addition to the surface mobility of adatoms contributing to NP architecture *via* GR, Au *et al.* showed that reaction stoichiometry can also contribute to overall NP architecture.[27] Specifically, they compared the titration of Ag nanocubes with an aqueous solution of $AuCl_4^-$ to that of $AuCl_2^-$ and found that porous AuAg nanocages were produced compared to solid-wall AuAg nanoboxes. The different products were attributed to the different reaction stoichiometries, where a greater number of Ag atoms are oxidized and removed from the template NPs per Au atom deposited in the case of $AuCl_4^-$, leading to porosity.

Here, we report the effect of reaction stoichiometry on NP architecture in a model system where metal heterostructures form rather than alloy NPs. We hypothesized that reaction stoichiometry would impact the structural evolution, with more metal islands (domains) forming per NP template when the local concentration of adatoms is higher. This hypothesis is tested in a model system wherein i-PdCu NPs undergo GR with either $AuCl_4^-$ or $AuCl_2^-$. Both $AuCl_4^-$ ($AuCl_4^-/Au$ E_{red} = 0.93 V *vs.* SHE) and $AuCl_2^-$ ($AuCl_2^-/Au$ E_{red} = 1.15 V *vs.* SHE) are thermodynamically capable of oxidizing and replacing both Pd ($PdCl_4^{2-}/Pd$ E_{red} = 0.59 V *vs.* SHE) and Cu (Cu/Cu^+ E_{red} = 0.52 V *vs.* SHE, Cu^{2+}/Cu E_{red} = 0.34 V *vs.* SHE) from the i-PdCu NPs, creating i-PdCu–Au heterostructures in which catalytic and plasmonic domains are joined together. The anticipated processes from GR are shown in eqn (1)–(4), highlighting the different reaction stoichiometries.

$$3\,Pd(s) + 2\,AuCl_4^-(aq) \rightarrow 3\,PdCl_2(aq) + 2\,Au(s) + 2\,Cl^-(aq) \quad (1)$$

$$Pd(s) + 2\,AuCl_2^-(aq) \rightarrow PdCl_2(aq) + 2\,Au(s) + 2\,Cl^-(aq) \quad (2)$$

$$3\,Cu(s) + 2\,AuCl_4^-(aq) \rightarrow 3\,CuCl_2(aq) + 2\,Au(s) + 2\,Cl^-(aq) \quad (3)$$

$$Cu(s) + 2\,AuCl_2^-(aq) \rightarrow CuCl_2(aq) + 2\,Au(s) + 2\,Cl^-(aq) \quad (4)$$

As reported herein, multiple Au islands are observed in the case of GR reaction with $AuCl_2^-$ and single Au islands occur in the case of $AuCl_4^-$ as depicted in Scheme 1.

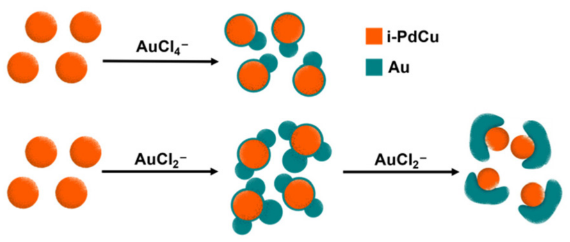

Scheme 1 Diagram detailing structural differences of the heterostructured NPs generated from the GR of i-PdCu NPs with a solution of (top) $AuCl_4^-$ and (bottom) $AuCl_2^-$.

Experimental

Materials

Oleylamine (70%, OLA), oleic acid (90%, OA), trioctylphosphine (97%, TOP), copper(II) acetate ($Cu(ac)_2$), palladium(II) bromide ($PdBr_2$), gold(I) chloride (AuCl), gold(III) chloride trihydrate ($HAuCl_4·3H_2O$), sodium chloride (NaCl), sodium hydroxide (NaOH), and cetyltrimethylammonium bromide (CTAB, 99%, lot BCCF7530) were purchased from Sigma-Aldrich and used as received. Nanopure water (18.2 MΩ cm) was used for all phase transfer processes and GR.

Methods

Synthesis of i-PdCu NPs. The i-PdCu NPs were synthesized as previously described by the Skrabalak group.[28] To a 100 mL round-bottom flask, 36 mg of $Cu(ac)_2$, 54 mg of $PdBr_2$, 18 mL of OLA, and 40 µL of OA were added, and this mixture was heated under vacuum to 110 °C with a heating mantle and held for 10 min with stirring. Then, 60 µL of TOP was added, and the solution was heated to 235 °C under Ar and held at this temperature for 30 min. The solution was allowed to cool to 70 °C temperature naturally and then the solution was transferred to a centrifuge tube along with 20 mL of hexane. The solution was centrifuged at 3900 RPM for 10 minutes to remove the larger particles by discarding the pellet. The supernatant with NPs was then precipitated out by ethanol and collected by centrifugation at 10 000 RPM for 10 minutes. The particles were then resuspended in 5 mL of hexane for future use.

Phase transfer. The phase transfer procedure of i-PdCu NPs from organic to aqueous solution is from a modified literature protocol.[29] First, 250 µL of hexane-suspended i-PdCu NPs were added to microcentrifuge tubes. The hexane was evaporated under the air. Then, 250 μL of OLA was added, followed by brief sonication. Next, 850 μL of 25 mM CTAB solution (in EtOH : H_2O 2 vol : 1 vol) was added. The microcentrifuge tubes were inverted several times and vortexed until a homogeneous solution by visualization formed. The solution was centrifuged for 15 min at 15 000 RPM. After centrifugation, the supernatant was carefully removed so that OLA can be discarded. The pellet was resuspended in 500 μL of nanopure H_2O. To remove ethanol, the resulting solution was heated at 70 °C under air for 30 min. To keep particle concentration constant across all experiments, several phase transfers were done in parallel, and NPs were combined after checking their sizes.

Galvanic replacement. GR reactions of i-PdCu template with $AuCl_2^-$ and $AuCl_4^-$ were done based on a modified literature procedure.[30] In a typical GR reaction, 800 μL of i-PdCu NPs (Multiple batches of i-PdCu were synthesized, characterized, and combined. All GR reactions mentioned in this article are done from the same big batch of i-PdCu. Approx 3.5 mg of i-PdCu NPs (in 800 μl of solution) was dispersed in 5 mL 4.5 mM CTAB solution in a 50 mL flask under magnetic stirring (*egg* shaped stir bar VWR catalog # 58949–010) and then heated to 100 °C using a heating mantle. Meanwhile, 0.1 mM $AuCl_4^-$ or 0.1 mM $AuCl_2^-$ titrants were prepared. At high concentrations, $AuCl_2^-$ undergoes disproportionation to a mixture of $AuCl_4^-$ and metallic gold.[31] To avoid such disproportionation, AuCl was washed three times with chloroform and dried in a vacuum overnight and freshly prepared solutions were used.[27] As AuCl has poor solubility in water, AuCl was dissolved in a saturated NaCl solution. Specific amounts of titrants were added to the flask through a syringe pump (KD scientific LEGATO 200) at a rate of 0.75 mL min^{-1} under magnetic stirring. The solution was heated for another 10 min after the titrant was finished being injected and removed from the heating mantle to cool. The sample was collected by centrifugation of the reaction media (15 min at 15 000 RPM). The collected pellet was washed several times with water and centrifugation to remove NaCl and finally redispersed in 500 μL H_2O.

Characterization methods. Transmission electron microscopy (TEM) images and selected area electron diffraction (ED) of NPs were taken on a JEOL 1400Plus transmission electron microscope operating at 120 keV and images were collected with a CMOS camera (Oneview camera, Gatan). High-magnification TEM (HR-TEM) images, coherent nano-area ED, electron tomography, and scanning TEM energy-dispersive X-ray spectroscopy (STEM-EDS) images were collected with JEOL JEM 3200FS microscope operating at 300 keV using a 4k × 4k GatanUltraScan 4000 CCD camera. The JEOL JEM 3200FS was interfaced with an Oxford Silicon Drift Detector for energy-dispersive X-ray spectroscopy (EDS). All samples for TEM and STEM imaging were prepared by dropcasting onto carbon-coated Cu and Mo grids (Ted Pella) respectively. Tomography tilt series were acquired from −70° to +70° with the serialEM software. The tilt increments were 1° each. The tilt series were recorded on a 4k × 4k Gatan UltraScan 400 CCD camera. The tomography tilt series were processed by the eTomo program from the IMOD package.[32] The tomogram was generated by aligning the image stack through cross-correlation and boundary model creation followed by 3D reconstruction through the Back projection method. UCSF ChimeraX software is used to visualize the generated tomograms.[33]

The NPs were also characterized by high-angle annular darkfield–scanning transmission electron microscopy (HAADF–STEM) and EDS on a ThermoFisher Scientific Themis Z TEM/STEM instrument operated at 300 keV. The instrument is equipped with a high-brightness Schottky 'extreme' field emission gun (XFEG) electron source, an electron energy monochromator, and a 5th-order probe spherical aberration corrector (DCOR). These features enabled STEM with sub-Angstrom imaging spatial resolution and provided ready access to high probe current for high-throughput EDS spectral mapping without the introduction of aberrations. The instrument is also installed with the ThermoFisher Scientific Super-X EDS system, which has four large areas (50 mm^2 each) silicon drift detectors (SDDs) with a large EDS collection solid angle of 0.7 Sr. These features along with a modern image drift correction algorithm in the Thermo Scientific Velox (v2.10) acquisition software enabled collection of clean EDS spectra and high spatial resolution spectral mapping of the NPs. A sample was prepared by dropcasting the colloidal NPs suspended in hexane onto carbon-coated Mo grids, followed by drying the sample in air and gentle plasma cleaning. The sample-bearing grid was loaded on a high-visibility double-tilt (HVDT) TEM specimen holder designed for EDS measurements. An electron beam with a high probe current of 500 pA was used for acquiring spatial maps of EDS spectra. The spatial maps of EDS spectra were converted into elemental composition maps with the aid of Thermo Scientific Velox (v2.10) software processing module.

The atomic percentages were determined by scanning electron microscopy-energy-dispersive X-ray spectroscopy (SEM-EDS) with Zeiss Auriga 60 FIB-SEM equipped with the X-Max 50 mm^2 silicon drift detector and the AZtec software package (Oxford Instrument).

The sizes of the NPs were determined using an automated MATLAB code measuring the contrast difference between the NPs and the background; more information can be found in the work reported by Harak *et al.*[34] Some NPs were measured manually in ImageJ.

The pH was measured with a VWR sympHony pH meter calibrated before use using standard buffer solutions.

Results and discussion

Monodisperse i-PdCu NPs were synthesized according to a modified literature procedure and had an average size of 9.8 ± 0.5 nm (Fig. S1A and B†).[28] These oleylamine-capped NPs were then transferred to an aqueous medium by using an ethanol and water solution with hexadecyltrimethylammonium bromide (CTAB), which is an amphiphilic ligand.[29] The morphology and size of the NPs were unchanged after the phase-transfer process (Fig. S1C and D†). Then, the aqueous suspensions of i-PdCu NPs were titrated with either aqueous $AuCl_4^-$ or $AuCl_2^-$ solutions at an injection rate of 0.75 mL min^{-1} at reflux. Due to the low solubility of AuCl in water, NaCl saturated water was used to dissolve AuCl through the formation of $NaAuCl_2$, which is water-soluble.

The collected products were characterized by TEM, showing different NP heterostructures from different volumes of $AuCl_4^-$ (Fig. 1A–C) and $AuCl_2^-$ (Fig. 1D–F) added while keeping the i-PdCu solution concentrations (*i.e.*, NP amount) constant. To show more explicitly the effect of reaction stoichiometry on NP architecture, Fig. 1 compares the products obtained when the volume of $AuCl_2^-$ solution added was three times that of $AuCl_4^-$ solution. This volume variation was designed judicially to maintain a constant number of electron exchanges for both reactions (Au available for replacement of Cu or Pd constant) while not having to change the rate of addition as a change in Au salt concentration would require. When 0.5 mL and 1.5 mL of $AuCl_4^-$ and $AuCl_2^-$ solutions are added, the quasi-spherical i-PdCu NPs are largely unchanged in terms of morphology. The average NP sizes decrease slightly to 9.2 ± 0.3 nm and 8.5 ± 0.4 nm, respectively (Fig. 1A and D). Increasing the volumes of titrant to 1.5 mL and 4.5 mL for $AuCl_4^-$ and $AuCl_2^-$, respectively, NPs with different domains become evident. In the case of $AuCl_4^-$ addition, the majority of NPs show two domains, adopting heterodimer structures consistent with previous results (Fig. 1B).[26] For $AuCl_2^-$ addition, heterodimers form but many of the NPs have multiple metal domains (Fig. 1E). As the volumes of titrant are increased to 3 mL and 9 mL for $AuCl_4^-$ and $AuCl_2^-$, respectively, the overgrowth domains become larger, but in the case of $AuCl_2^-$, structures with multiple domains dominate the sample (Fig. 1F).

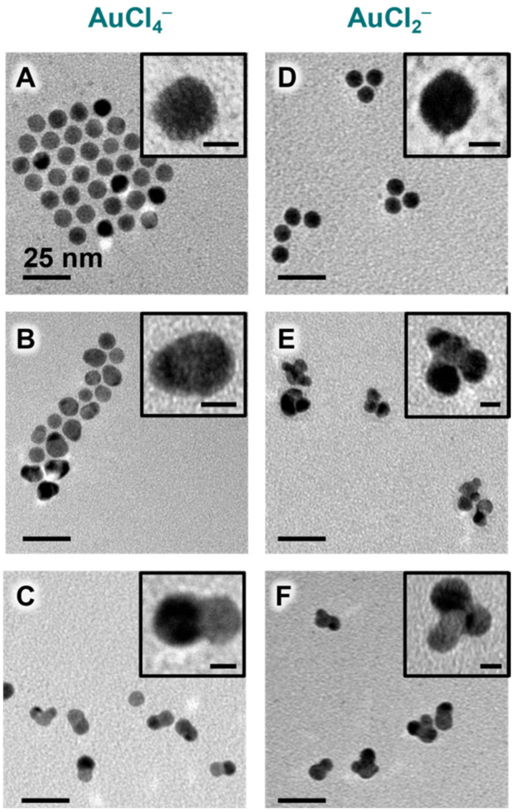

Fig. 1 TEM images of products obtained from GR between i-PdCu NPs and (A) 0.5, (B) 1.5, and (C) 3 mL of 0.1 mM $AuCl_4^-$ or (D) 1.5, (E) 4.5, and (F) 9 mL of 0.1 mM $AuCl_2^-$. Scale bars = 25 nm for all (inset scale bars = 5 nm).

Given the different NP morphologies obtained with $AuCl_2^-$ compared to $AuCl_4^-$, a large volume of $AuCl_2^-$ was added to the i-PdCu NPs to understand the extent to which replacement can proceed in this system. TEM images show that the addition of 25 mL of $AuCl_2^-$ solution resulted in boat-shaped dimers (Fig. S2E†), a morphology different from when a large volume of $AuCl_4^-$ has been added as published previously.[26] This boat-like morphology of the i-PdCu–Au heterostructures is further supported by electron tomography (Fig. S3, ESI video 1†).

Examination of the TEM images in Fig. 1, however, reveals a mixture of nanostructures, *i.e.*, NPs at different stages of exchange. These NP images were analyzed further to understand what structures dominate at each stage and quantified according to their domain number and shape (n ∼ 100; Fig. 2A). With the increase of $AuCl_4^-$ solution from 0.5 mL to 3 mL, the GR reaction NPs morphology shifts from quasi-spheres to dimer-like structures (Fig. 2B–D). In contrast, increasing $AuCl_2^-$ solution from 0.5 mL to 9 mL shifts the morphology of the GR product from quasi-spheres to dimers to NPs with multiple domains (Fig. 2E–H). Finally, upon addition of 25 mL of $AuCl_2^-$ solution results in heterostructured NPs with one large domain but with a boat-like morphology and a small spherical part inside the concavity (Fig. 2I). These results also show that, while the starting point (Fig. 2B and E) and end samples in both cases are nearly monodisperse (Fig. 2D and I), intermediate samples are polydisperse, indicating that nucleation of the new phase(s) occurs at different time points depending on the specific template NP (Fig. S4–S11†).

Reaction parameters that can influence GR include temperature, duration of reaction, rate of titrate addition, concentration of titrant, and volume of titrant.[18] A complete description of the parameters for each of the above-mentioned GR reactions is presented in Table S1.† A control experiment was designed to see if the $AuCl_2^-$ titrant's concentration affects the different domains. In this experiment instead of three times more volume of $AuCl_2^-$ solution, three times more concentrated $AuCl_2^-$ solution was used. The TEM images of GR products from 1.5 mL of 0.3 mM $AuCl_2^-$ solution show NPs with multiple domains. Interestingly, the domains are not as large or protruding as the product from the 0.1 mM $AuCl_2^-$ solution, indicating that addition rate and total reaction time are important to domain formation (Fig. S12†). In the present work, temperature, the concentrations of both titrant solutions, and the rate of titrant addition were kept constant. Additionally, the effect of Cl^- concentration was also probed as the $AuCl_2^-$ solution is saturated with NaCl while the $AuCl_4^-$ solution was not in the original $AuCl_4^-$ experiments. Specifically, 3 mL of NaCl-saturated 0.1 mM $AuCl_4^-$ solution was titrated with an

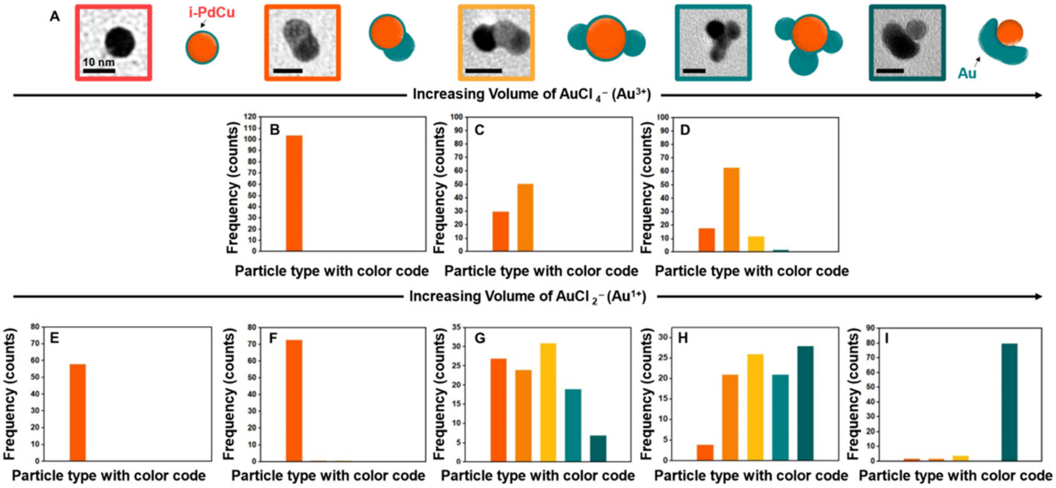

Fig. 2 (A) TEM images of different i-PdCu–Au NPs observed from GR between i-PdCu NPs and Au solutions ($AuCl_4^-$ and $AuCl_2^-$), with structural models adjacent. The outline of each TEM image serves as a color code to denote the particle type in parts B–E. Scale bars = 10 nm. Histograms of NPs (n∼100) with different Au domains as i-PdCu NPs were titrated with (B) 0.5 mL, (C) 1.5 mL, (D) 3 mL of 0.1 mM $AuCl_4^-$ solution, and (E) 0.5 mL, (F) 1.5 mL, (G) 4.5 mL, (H) 9 mL, and (I) 25 mL of 0.1 mM $AuCl_2^-$ solution.

equal quantity of i-PdCu NPs. Dimer-like NPs are produced, with all characterization consistent with the original system (Fig. S13† *vs.* Fig. 1C). These results indicate the differences in morphology do not arise from the differences in Cl^- concentration.

Further, the effect of pH was studied as the 0.1 mM solutions of $AuCl_4^-$ and $AuCl_4^-$ were measured to be 6.6 and 3.5, respectively, and can impact the solution speciation.[35] Specifically, $AuCl_4^-$ complexes are hygroscopic and can undergo spontaneous stepwise hydrolysis at different pHs which can alter E_{red}. However, at pH 3.5, $AuCl_4^-$ species dominate over hydrolysed species.[36] $AuCl_2^-$ is not hygroscopic, forming $NaAuCl_2$ in NaCl-saturated water, and does not hydrolyze depending on pH. Still, two control experiments were undertaken to better understand the effect of pH on our system. Specifically, the pH of $AuCl_4^-$ solutions were altered to 7.4 and 12.5 using NaOH, keeping the Au concentration at 0.1 mM; these solutions were then titrated into the i-PdCu NP solution at standard conditions. TEM images of GR products of pH 7.4 solution show heterostructured NPs consistent with one Au domain, which is similar to the products obtained at pH 3.5 (Fig. S14†). The i-PdCu NPs appear unaltered from the titration of the $AuCl_4^-$ solution adjusted to pH 12.5 (Fig. S15†). Bulk elemental analysis of this reaction product by SEM-EDS shows no Au signals upon AutoID and the diameters of the NPs before (8.3 ± 0.5 nm) and after (8.5 ± 0.9 nm) are also similar. These results are expected as $Au(OH)_4^-$ species dominate at high pH, shifting the titrant to one with a lower reduction potential ($Au(OH)_4^-/Au$ E_{red} = 0.6 V *vs.* SHE).[36,37] Taken together, these results indicate that pH is an important consideration but does not impact the major conclusions of this study.

The products produced from GR of i-PdCu titrated with two different gold titrant solutions were further characterized by STEM-EDS (Fig. 3).[26] For comparison and identification of the various phases in the nanostructures produced in the $AuCl_2^-$ system, this characterization was also accompanied with ED (Fig. S16†). Prior to the addition of $AuCl_2^-$, ED confirmed the intermetallic phase of the initial NPs (Fig. S16A†). With 1.5 mL of $AuCl_2^-$ titrant, the NPs are largely quasi-spherical, with a weak Au signal at the periphery of the NPs evident by STEM-EDS (Fig. 3A). Additional images supporting the deposition of a Au-rich shell are shown in Fig. S17A.† More noticeable is the enrichment of Pd near the surface of the NP, suggesting that Cu is being removed at a greater rate in the early stages of GR.

With 4.5 mL of $AuCl_2^-$ titrant, quasi-spherical core@shell i-PdCu@Au NPs are also noticeable, along with i-PdCu–Au heterostructures with one or two domains. A possibly discontinuous or alloyed shell is visible irrespective of morphology and number of domains (Fig. S17B and C†). STEM-EDS (Fig. 3B) shows the brighter domain mainly consists of Au with little Cu and Pd and the darker domain contains Pd and Cu. The same samples are analyzed further, especially the intersection of the Au domain with i-PdCu. STEM-EDS line scan analysis shows that Pd is greater toward the Au intersection zone (Fig. S18A–C†). The other i-PdCu–Au heterostructure NPs with multiple (two or three) domains were also analyzed and show similar Pd localization and Au shell (Fig. S18D–I†).

In the next stage of the GR reaction, where 9 mL of $AuCl_2^-$ was added, i-PdCu–Au NP heterostructures with mainly two or three Au domains are observed as shown in Fig. 3C and D, respectively. ED of this GR product shows the diffraction rings for i-PdCu as well as face-centered cubic (FCC) Au, confirming the preservation of the intermetallic phase of the original i-PdCu NPs as well as the new Au phase (Fig. S16C†). Finally, when 25 mL of $AuCl_2^-$ is titrated against i-PdCu, STEM-EDS of the boat-like i-PdCu–Au heterostructures (Fig. S2E and S11†)

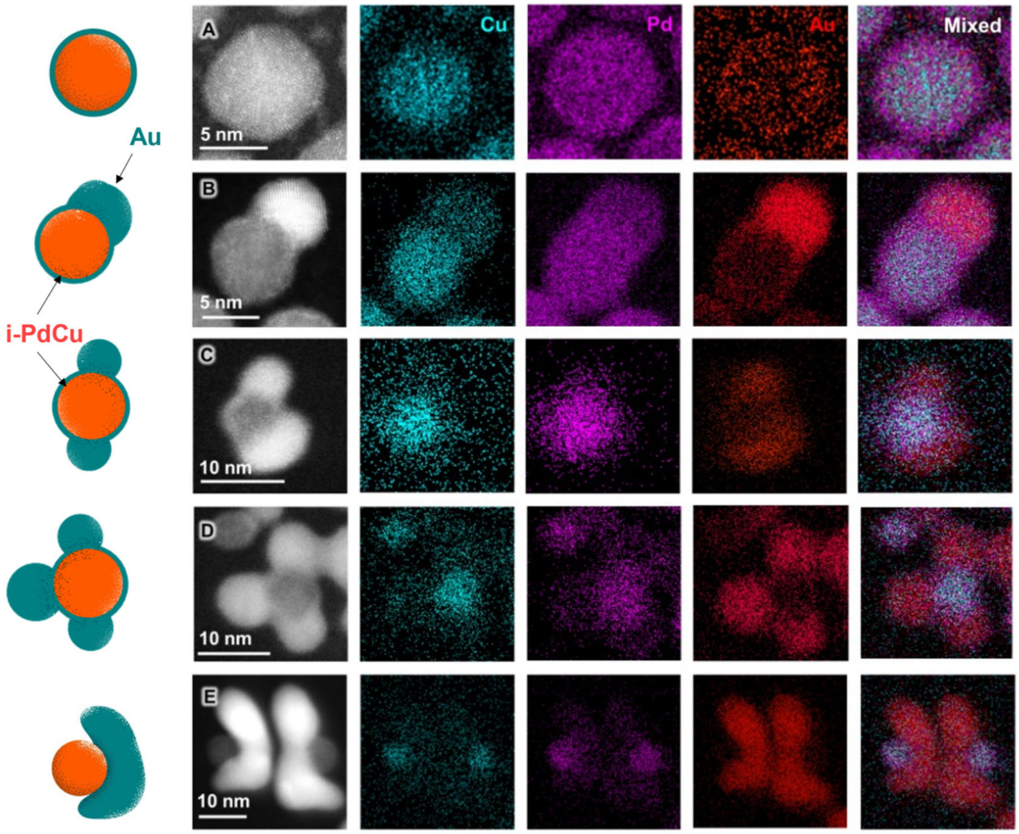

Fig. 3 (Left-right) Models, HAADF-STEM images, and STEM-EDS maps of products from GR of i-PdCu NPs titrated with (A) 1.5 mL (no domain core@-shell i-PdCu@Au), (B) 4.5 mL (one domain), (C) 9 mL (two domains), (D) 9 mL (three domains), and (E) 25 mL (boat-shaped) of 0.1 mM $AuCl_2^-$ solution.

shows that the boat-like large domain mostly contains Au, with Pd and Cu in the NP at the concavity (Fig. 3E). The Au shell around i-PdCu is not observed at this stage of GR.

This multi-domain formation is in contrast to the GR result with $AuCl_4^-$; in the case of $AuCl_4^-$, only NPs with a single Au domain form (Fig. S19†).[26] ED of the GR products shows the presence of i-PdCu as well as the FCC Au phase (Fig. S16B†).

Along with the microscopic analysis, bulk elemental analysis was obtained using SEM-EDS. Table S2† summarises the data, showing an increase of Au atomic percentage (at%) with the increasing volume of $AuCl_2^-$ or $AuCl_4^-$ solution added. When 0.5 mL of either $AuCl_2^-$ or $AuCl_4^-$ solution was added, a similar Au at% of ∼1.7% was obtained, suggestive of similar extents of exchange. This observation continues with increasing volumes of $AuCl_2^-$ and $AuCl_4^-$ solutions, with minor deviations. This variability increases slightly as the reaction proceeds, which we attribute to heterogeneity from one particle to the next as samples contain particles at different extents of exchange until large volumes have been added. As the at% of Au increases in the GR products, the Pd : Cu ratio changes with either titrant (Fig. 4). For both $AuCl_4^-$ and $AuCl_2^-$, the nanostructures first become enriched with Pd relative to Cu (Fig. 4B and D), indicating that Cu is being replaced by Au more quickly than Pd. However, the Pd : Cu ratio decreases at high volumes of $AuCl_4^-$ solution added. We note that absolute values of Au, Cu, and Pd during the exchange process are not available due to the small amount of i-PdCu NPs used in each exchange experiment.

i-PdCu–Au heterostructure mechanisms

Depending on the energies of interface formation, three different growth modes can be observed: (i) Frank–van der Merwe (FM; layer-by-layer growth), (ii) Volmer–Weber (VW; island growth), and (iii) Stranski–Krastanov (SK; mixed mode growth).[38] FM deposition is favorable when the deposited metal and the seed have a small lattice mismatch. Still, a strained conformal layer can develop when the difference in lattice constants is high; however, island growth will take over when the deposited layers are sufficiently thick because there will no longer be an energy gain for wetting (*i.e.*, SK growth mode). VW mode is common when depositing metal has a significant lattice mismatch with the underlying surface (*i.e.*, seed). Looking at the STEM-EDS data at the early stages of GR between i-PdCu and both Au salts, we note that a thin shell of Au forms first. Then, with further Au addition, islands are observed, which is consistent with the SK mode. The lattice mismatch in this Au depositing system is high assuming an interface between i-PdCu{100} and FCC Au{111} as reported before.[26] However, the elemental map and microscopic characterization reveal Pd enrichment at the i-PdCu and Au domain

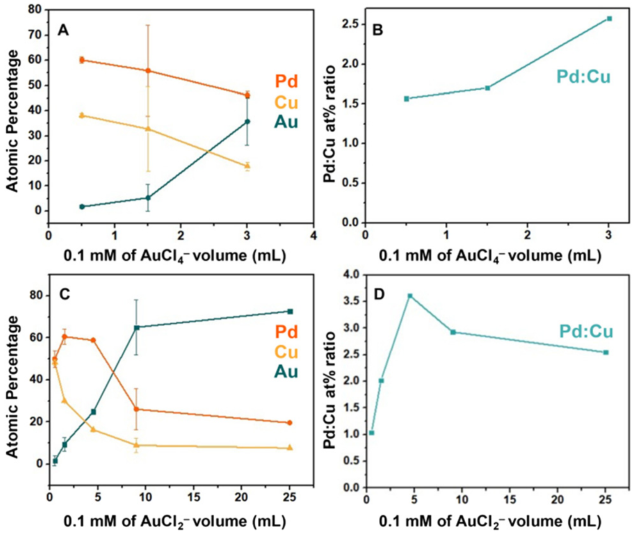

Fig. 4 (A–C) Plot of titrant volume *vs.* atomic percentages showing the evolution of atomic percentage determined by SEM-EDS of Pd, Cu, and Au, (B–D) plot of titrant volume *vs.* Pd : Cu atomic percentage ration showing the evolution of Pd, Cu ratio in i-PdCu system.

interface, which can reduce the lattice mismatch. While our results are consistent with SK growth, we do acknowledge that this model was developed for explaining the deposition of 2D films on planar substrates, which our system lacks. Whether such a description extends to high curvature NPs is unclear at this stage of development as Niu *et al.* showed GR of noble metal (Ag, Au) with active metal (Mg, Zn) "spherical" NPs results in nanoscale heterostructures *via* the Volmer–Weber growth mode.[39]

The bond energies between the adatoms and the substrate layer also contribute to the growth mode. STEM-EDS and line scan profiles (Fig. S18 and S19†) show that not only the exterior of the NP is Pd rich but also the intersection of the i-PdCu and Au domains is Pd rich. Notably, the Au–Au bond energy or bond dissociation energy (BDE) is 226.2 kJ mol^{-1} which is higher than the Au–Pd BDE (142.7 kJ mol^{-1}). The higher Au–Au bond energy may also contribute to why Au islands are observed rather than continuation of the conformal Au shell, supporting the SK growth mode.

Finally, the deposition mode of one metal on another substrate can depend also on the rates of deposition and surface diffusion of adatoms. Xia *et al.* have shown that the rates of atom deposition and surface diffusion can be controlled to achieve Pd nanocrystals of different shapes.[25] Similar outcomes were accomplished in the bimetallic system when Rh was deposited on Pd NP seeds.[40] In the results presented here, the deposition rate depends on the number of Au adatoms generated, as no external reducing agent is used. From eqn (1)–(4), it is evident that changing the titrant to AuCl$_2^-$ from AuCl$_4^-$ changes the stoichiometry of the GR process. That is, oxidation of 3 Pd/Cu atoms will generate 2 Au^0 adatoms from AuCl$_4^-$ and 6 Au^0 adatoms from AuCl$_2^-$. Recall that in our experiments, 3 times more AuCl$_2^-$ is added so that the number of electrons participating is constant at a given volume of titrant. Therefore, at the same time point, more Au adatoms will be generated with AuCl$_2^-$. As the number of adatoms is more, the local supersaturation of the reaction mixture increases, and the deposition rate of adatoms will be higher. Such conditions decrease the barrier for nucleation and the critical nuclei size decreases, which may account for why more Au domains are observed with AuCl$_2^-$ compared to AuCl$_4^-$ as a titrant. For AuCl$_4^-$, the slower deposition rate will give more time for adatom diffusion, giving rise to fewer domains. Overall, the comparison of AuCl$_2^-$ and AuCl$_4^-$ as oxidants for GR of i-PdCu indicates that the reaction stoichiometry contributes to the architecture of heterostructured NPs by directing the flux of adatoms relative to surface diffusion.

Conclusions

By changing the reaction stoichiometry of a GR process, we have shown that the architecture of heterostructured NPs can be tuned from having a single overgrowth domain to multiple overgrowth domains. This outcome was demonstrated by titrating i-PdCu NPs with either AuCl$_2^-$ or AuCl$_4^-$. The former produced NPs with multiple Au domains while the latter produced NPs with single Au domains. These structures are explained in context with standard thin film growth modes, indicating that the stoichiometry of a GR reaction is an important parameter to control the flux of adatoms and, thus, overall NP architecture. These results enable GR to be more predictably used to achieve complex NPs with different material domains and functions, in this case coupling a plasmonic metal (Au) with a catalytic domain (i-PdCu).

Author contributions

N. K. and S. E. S. were responsible for the project concept and design of experiments. N. K. developed the synthesis of i-PdCu NPs, Phase transfer, galvanic replacement product: i-PdCu-Au heterostructured NPs, characterizations and wrote the article. M. M. and J. W. helped in i-PdCu NPs synthesis and some control experiments respectively. Z. W. assisted with elemental characterization *via* some STEM-EDS maps. X. Z. helped in tomography experiments. This manuscript was written through the contributions of all authors. All authors have given approval to the final version of this Manuscript.

Conflicts of interest

The authors declare no competing financial interest.

Acknowledgements

S. E. S., N. K., M. M., and J. W. acknowledge financial support from Indiana University and the US National Science Foundation (NSF CHE 1904499 and 2203349). The authors acknowledge support from Indiana University's Electron Microscopy Center and Nanoscale Characterization Facility for access to instrumentation. The aberration-corrected STEM measurements were carried out in the Materials Research Laboratory Central Research Facilities, the University of Illinois at Urbana-Champaign.

References

1 C. Wang, H. Daimon and S. Sun, *Nano Lett.*, 2009, **9**, 1493–1496.

2 N. Razgoniaeva, P. Moroz, S. Lambright and M. Zamkov, *J. Phys. Chem. Lett.*, 2015, **6**, 4352–4359.

3 X. Liu, W. Li, N. Chen, X. Xing, C. Dong and Y. Wang, *RSC Adv.*, 2015, **5**, 34456–34465.

4 C. W. Kim, S. P. Suh, M. J. Choi, Y. S. Kang and Y. S. Kang, *J. Mater. Chem. A*, 2013, **1**, 11820–11827.

5 L. Amirav, F. Oba, S. Aloni and A. P. Alivisatos, *Angew. Chem., Int. Ed.*, 2015, **54**, 7007–7011.

6 U. Banin, Y. Ben-Shahar and K. Vinokurov, *Chem. Mater.*, 2014, **26**, 97–110.

7 Q. Q. Dou, A. Rengaramchandran, S. T. Selvan, R. Paulmurugan and Y. Zhang, *Sci. Rep.*, 2015, **5**, 8252.

8 L. Dong, P. Zhang, X. Liu, R. Deng, K. Du, J. Feng and H. Zhang, *ACS Appl. Mater. Interfaces*, 2019, **11**, 7774–7781.

9 J. L. Fenton, B. C. Steimle and R. E. Schaak, *Science*, 2018, **360**, 513–517.

10 J. Zhu, B. Zhang, J. Tian, J. Wang, Y. Chong, X. Wang, Y. Deng, M. Tang, Y. Li, C. Ge, Y. Pan and H. Gu, *Nanoscale*, 2015, **7**, 3392–3395.

11 X. Ding, Y. Zou, F. Ye, J. Yang and J. Jiang, *J. Mater. Chem. A*, 2013, **1**, 11880–11886.

12 G. Wu, J. Zhu, G. Weng, J. Li and J. Zhao, *Microchim. Acta*, 2021, **188**, 345.

13 W. Ma, M. Sun, L. Xu, L. Wang, H. Kuang and C. Xu, *Chem. Commun.*, 2013, **49**, 4989–4991.

14 T. A. Gschneidtner, S. Lerch, E. Olsén, X. Wen, A. C. Y. Liu, A. Stolaś, J. Etheridge, E. Olsson and K. Moth-Poulsen, *Nanoscale*, 2020, **12**, 11297–11305.

15 M. R. Buck, J. F. Bondi and R. E. Schaak, *Nat. Chem.*, 2011, **4**, 37–44.

16 A. Ohnuma, E. C. Cho, P. H. C. Camargo, L. Au, B. Ohtani and Y. Xia, *J. Am. Chem. Soc.*, 2009, **131**, 1352–1353.

17 N. Ortiz and S. E. Skrabalak, *Langmuir*, 2014, **30**, 6649–6659.

18 X. Xia, Y. Wang, A. Ruditskiy and Y. Xia, *Adv. Mater.*, 2013, **25**, 6313–6333.

19 S. E. Skrabalak, J. Chen, Y. Sun, X. Lu, L. Au, C. M. Cobley and Y. Xia, *Acc. Chem. Res.*, 2008, **41**, 1587–1595.

20 Y. Sun and Y. Xia, *Nano Lett.*, 2003, **3**, 1569–1572.

21 A. G. M. da Silva, E. A. Lewis, T. S. Rodrigues, T. J. A. Slater, R. S. Alves, S. J. Haigh and P. H. C. Camargo, *Chem. – Eur. J.*, 2015, **21**, 12314–12320.

22 L. Castilla-Amorós, D. Stoian, J. R. Pankhurst, S. B. Varandili and R. Buonsanti, *J. Am. Chem. Soc.*, 2020, **142**, 19283–19290.

23 X. Wang, S. Chen, G. Reggiano, S. Thota, Y. Wang, P. Kerns, S. L. Suib and J. Zhao, *Chem. Commun.*, 2019, **55**, 1249–1252.

24 Y. Xia, X. Xia and H.-C. Peng, *J. Am. Chem. Soc.*, 2015, **137**, 7947–7966.

25 X. Xia, S. Xie, M. Liu, H.-C. Peng, N. Lu, J. Wang, M. J. Kim and Y. Xia, *Proc. Natl. Acad. Sci. U. S. A.*, 2013, **110**, 6669–6673.

26 A. N. Chen, E. J. Endres, H. M. Ashberry, S. L. A. Bueno, Y. Chen and S. E. Skrabalak, *Nanoscale*, 2021, **13**, 2618–2625.

27 L. Au, X. Lu and Y. Xia, *Adv. Mater.*, 2008, **20**, 2517–2522.

28 C. Wang, X. Sang, J. T. L. Gamler, D. P. Chen, R. R. Unocic and S. E. Skrabalak, *Nano Lett.*, 2017, **17**, 5526–5532.

29 L. Wu, J. Yu, L. Chen, D. Yang, S. Zhang, L. Han, M. Ban, L. He, Y. Xu and Q. Zhang, *J. Mater. Chem. C*, 2017, **5**, 3065–3071.

30 S. E. Skrabalak, L. Au, X. Li and Y. Xia, *Nat. Protoc.*, 2007, **2**, 2182–2190.

31 C. H. Gammons, Y. Yu and A. E. Williams-Jones, *Geochim. Cosmochim. Acta*, 1997, **61**, 1971–1983.

32 J. R. Kremer, D. N. Mastronarde and J. R. McIntosh, *J. Struct. Biol.*, 1996, **116**, 71–76.

33 E. F. Pettersen, T. D. Goddard, C. C. Huang, G. S. Couch, D. M. Greenblatt, E. C. Meng and T. E. Ferrin, *J. Comput. Chem.*, 2004, **25**, 1605–1612.

34 E. W. Harak, K. M. Koczkur, D. W. Harak, P. Patton and S. E. Skrabalak, *ChemNanoMat*, 2017, **3**, 815–821.

35 M. D. Susman, R. Popovitz-Biro, A. Vaskevich and I. Rubinstein, *Small*, 2015, **11**, 3942–3953.

36 J. R. Daniel, L. A. McCarthy, S. Yazdi, M. Chagnot, E. Ringe and D. Boudreau, *J. Phys. Chem. C*, 2018, **122**, 18168–18176.

37 S. G. Bratsch, *J. Phys. Chem. Ref. Data*, 1989, **18**, 1–21.

38 H.-C. Peng, S. Xie, J. Park, X. Xia and Y. Xia, *J. Am. Chem. Soc.*, 2013, **135**, 3780–3783.

39 K.-Y. Niu, S. A. Kulinich, J. Yang, A. L. Zhu and X.-W. Du, *Chem. – Eur. J.*, 2012, **18**, 4234–4241.

40 H. Zhang, W. Li, M. Jin, J. Zeng, T. Yu, D. Yang and Y. Xia, *Nano Lett.*, 2011, **11**, 898–903.